Journal of Materials Chemistry A

PAPER

View Article Online
View Journal | View Issue

Cite this: J. Mater. Chem. A, 2014, 2, 11382

Controlled mechanical cleavage of bulk niobium diselenide to nanoscaled sheet, rod, and particle structures for Pt-free dye-sensitized solar cells†

Mohammed Aziz Ibrahem,[abc] Wei-Chih Huang,[d] Tian-wey Lan,[ab] Karunakara Moorthy Boopathi,[be] Yu-Chen Hsiao,[d] Chih-Han Chen,[d] Widhya Budiawan,[ab] Yang-Yuan Chen,[f] Chia-Seng Chang,[f] Lain-Jong Li,[g] Chih-Hung Tsai*[d] and Chih Wei Chu*[eh]

Received 16th April 2014
Accepted 27th April 2014

DOI: 10.1039/c4ta01881h

www.rsc.org/MaterialsA

In this study, we report a one-step process for the preparation of $NbSe_2$ nanosheets, nanorods and nanoparticles from pristine materials under the effects of shear and friction forces. Nevertheless, simple and facile methods for the large-scale syntheses of well-defined $NbSe_2$ nanostructures in high yield have yet to be realized and that will have a great impact in a wide range of applications. For example, developing platinum (Pt)-free and highly efficient counter electrodes is meaningful and necessary for the cost reduction of dye-sensitized solar cells (DSSCs). By integrating this approach with a simple method of thin film preparation (spray coating) allowed us to prepare large-area, conductive, semitransparent flexible thin films of $NbSe_2$. We have used microscopic and macroscopic methods to examine the morphologies, compositions, crystallinity, and electrical and optical properties of the converted $NbSe_2$ nanostructures. DSSCs with $NbSe_2$ nanosheet counter electrodes (CEs) achieved a conversion efficiency of 7.73%, superior to an efficiency of 7.01% for Pt-based CEs. Our $NbSe_2$ nanostructure provides a cost-effective CE alternative to the noble metal Pt in DSSCs.

Introduction

Two-dimensional (2D) nanostructures have received much attention since the discovery of graphene in 2004.[1] In addition, transition metal dichalcogenides (TMDs), a group of 40 different types of inorganic layered compounds combining transition metals (M: W, Mo, Ti, Nb, Ta) and chalcogens (X: S, Se, Te)[2–4] in an MX_2 stoichiometry, are extremely promising building blocks for the development of many next-generation applications, including superlubricants,[5] superconductors,[6] batteries,[7] solar cells,[8] DSSCs,[9] thin-film transistors,[10,11] LEDs,[12] UV range photodetectors,[13] and transparent conducting electrodes.[14] Crystallographically similar to graphite, the sandwich layers are stacked together by van der Waals interactions; therefore, MX_2 species have the propensity to delaminate into individual nanosheets comprising only a few atomic layers. Depending on the combination of metals and chalcogens, TMDs can be metallic, semimetallic, or semiconducting; for example, tungsten sulfide (WS_2) and molybdenum sulfide (MoS_2) are usually semiconducting, while niobium selenide ($NbSe_2$) is metallic.[15] Among the TMDs, it has been demonstrated recently that the $NbSe_2$ precursor is a particularly excellent model system for processing and fabricating rich inorganic nanostructures using various methods.[16] The metallic behavior of $NbSe_2$ arises from the fact that within the sandwich layer each Nb atom is coordinated to six selenide atoms in the form of a trigonal prism (see Fig. S1, ESI†), similar to the corresponding structures of WS_2 and MoS_2, except that Nb has one d electron less than Mo or W in its valence shell; the Fermi energy is, therefore, shifted to the d band.[17]

Several synthesis techniques have been proposed over the past decade for the production of TMD nanostructures, including liquid exfoliation,[18,19] intercalation-assisted exfoliation,[20,21] chemical vapor deposition,[22] hydrothermal methods,[23,24] solvothermal methods,[25] microwave methods,[26] and mechanosynthesis (high energy ball-milling).[8] Generally, layered crystals can be synthesized to form highly anisotropic compounds that readily cleave along a preferred plane. Mechanically peeled 2D sheets typically feature fewer defects

[a]Department of Physics, National Taiwan University, Taipei 106, Taiwan
[b]Nanoscience and Technology Program, Taiwan International Graduate Program, Academia Sinica, Taipei 115, Taiwan
[c]Department of Physics, Faculty of Science, University of Duhok, Duhok, Iraq
[d]Department of Opto-Electronic Engineering, National Dong Hwa University, Hualien 97401, Taiwan. E-mail: cht@mail.ndhu.edu.tw
[e]Research Center of Applied Science, Academia Sinica, Taipei 115, Taiwan
[f]Institute of Physics, Academia Sinica, Taipei 115, Taiwan
[g]Institute of Atomic and Molecular Sciences Academia Sinica, Taipei 10617, Taiwan
[h]Department of Photonics, National Chiao Tung University, Hsinchu 300, Taiwan. E-mail: gchu@gate.sinica.edu.tw

† Electronic supplementary information (ESI) available. See DOI: 10.1039/c4ta01881h

than those produced using chemical methods.[27] If a mechanical process can be developed to treat tens of thousands of particles in a single run and to peel each particle hundreds of times, a large number of high-quality nanosheets could be harvested for studies of their properties and for their practical applications. For these reasons, there is a strong motivation for systematic and fundamental investigation of growth control mechanisms related to $NbSe_2$ parent compounds.

A typical DSSC consists of a transparent conductive substrate, a porous thin-film photoelectrode composed of TiO_2 nanoparticles, dyes, an electrolyte, and a CE.[28,29] The CE, an important component in DSSCs, is usually composed of a conductive catalytic layer. The requirements for the CE in DSSCs are low charge-transfer resistance and high exchange current densities for effective reduction of the oxidized species, and good chemical/electrochemical stability in the electrolyte systems.[30,31] Due to the high electrocatalytic activity and good chemical stability, in most cases Pt is used as the CE material to obtain high efficiency DSSCs. However, as a noble metal, Pt is relatively expensive, which is a big obstacle for the large-scale application of DSSCs.[9,30] Therefore, developing a Pt-free and highly efficient CE is meaningful and necessary for the cost reduction of dye-sensitized solar cells. Here, we have developed a simple but effective approach for exfoliating ultrathin nanosheets from bulk powder and then fracturing them into nanorods and finally breaking them into nanoparticles (nanoplatelets) in high yield through control over the imposing time in a one-step process. Because of its metallic prosperity, high electrocatalytic activity and reversibility in the I_3^-/I^- redox reaction, we used $NbSe_2$ nanostructures as Pt replacement CEs in DSSCs. Unlike previously reported approaches of TMD preparation, our solution-based method is rapid, easy, cheap, and insensitive to ambient conditions; it does not require a third-phase dispersant (*i.e.*, surfactant), it consumes low amounts of energy, and it can potentially be scaled up to give large quantities (liters) of dispersions of exfoliated materials (see Fig. S2, ESI†) exhibiting high stability over long periods of time (at least six months; see sedimentation tests in Fig. S3, ESI†). According to our knowledge, this is the first time that three different types (shape and size) of nanomaterials can be produced in a one-step process. Considering the generality of this simple realization of exfoliated $NbSe_2$ nanomaterials, our method might stimulate interest in the growth of a very broad range of TMD systems exhibiting various properties and functionalities. By integrating this approach with a simple method of thin film preparation allowed us to prepare large-area thin films. The results showed that DSSCs based on $NbSe_2$ nanosheet CEs achieved a higher efficiency than those based on Pt-based CEs.

Experimental section

Nanomaterial preparation

The homemade wet grinding machine used to prepare $NbSe_2$ nanomaterials is presented in Scheme S1.† First, $NbSe_2$ powder (99.9%; Alfa Aesar) was mixed with pure *N*-methyl-2-pyrrolidinone (NMP, 99% Macron Chemical, USA) at a concentration of 0.5 wt%. Approximately 50% of the container was filled with micro-sized zirconia beads (size, 100 μm; density, ~5.95 g cm^{-3}); the remaining volume was a suspension of the particles to be ground. The peripheral speed of the rotor was fixed at 2000 rpm. A water-cooled circulation allowed the temperature to be controlled during the size-reduction process. The bright red dispersion was purified without any contamination from the zirconia beads, which were highly dense and, therefore, precipitated readily after grinding to the bottom of the container.

Microscopic and spectroscopic observation

The ground dispersion of the nanomaterial was diluted ten-fold with isopropyl alcohol (IPA, 99%; Alfa Aesar); drops of the solution were placed on a holey carbon-coated copper grid (Lacey Carbon Type-A 300 mesh copper grid; TED Pella) or Si/SiO_2 and then dried in air at 70 °C prior to characterization using TEM (JEM 2100F), SEM (FEI Nova200), AFM (Veeco di Innova) coupled with XPS (PHI 5000 Versa Probe scanning ESCA microprobe), and Raman spectroscopy (NT-MDT confocal Raman microscopic system; excitation laser wavelength: 514 nm; laser spot size: 0.5 μm). TMD powders before and after grinding were characterized using XRD (PANalytical).

$NbSe_2$ thin film and CE fabrication

$NbSe_2$ nanomaterial thin films were fabricated by using a simple spray deposition method. The spray-coating set-up was developed in a conventional environment (air) under a chemical hood. We used a simple dual action commercial airbrush (MECAFER AG-1) supplied by a nitrogen line and fixed on a mechanic arm over a hot plate (for the control of substrate temperature during the spray). The PET substrates were cleaned in an ultrasonic bath with acetone and IPA (10 min each step). The dispersion of the nanomaterials was first diluted with IPA in a 1 : 1 ratio in order to speed up the drying process. The solution was pumped into the air stream in the spray nozzle continuously on the PET substrate. By controlling the nozzle diameter and adjusting the distance between the sample and sprayer head, very uniform thin films were fabricated. After the spray deposition, thin films were left in air for 1 h to dry. $NbSe_2$ CEs were fabricated by depositing $NbSe_2$ nanostructure materials on fluorine doped tin oxide (FTO) glass plates using the drop casting method. The FTO glasses coated with $NbSe_2$ were then annealed under a N_2 atmosphere at 500 °C for 30 min in a tube furnace to form $NbSe_2$ CEs. A Pt CE for the DSSC was prepared by coating the paste of chemical Pt precursor (platinum(II) acetylacetonate, 99.99% trace metals basis, Sigma-Aldrich) on FTO glass plates by the doctor-blade method. After heating at 450 °C for 20 minutes, a quasi-transparent activated Pt layer was obtained.

Magnetic susceptibility measurement

The zero-field-cool (ZFC) susceptibility measurement was performed by using a superconducting quantum interference device magnetometer (SQUID, Quantum Design Inc.). The samples were cooled in zero field from 0 K temperature in a

strong magnetic field (FC). Then the samples were heated gradually while measuring magnetization (M) with a constant field.

Electrical and optical measurements

The optical properties (absorption and transmittance spectra) of thin films were recorded using a Jasco V-670 UV-vis-NIR spectrophotometer. While the conductivities were measured at room temperature using the van der Pauw four-point probe technique with a Hall effect measurement system (Ecopia, HMS 5000).

Characterization of the CEs

Cyclic voltammetry (CV) was employed to characterize the relative catalytic ability of the CEs. CV measurements were conducted using a three-electrode electrochemistry system. Pt or $NbSe_2$ CEs under testing were used as the working electrodes, Pt foil as the counter electrode, and Ag/Ag^+ as the reference electrode. The scan rate used was 50 mV s^{-1}, while the electrolyte was the acetonitrile solution containing 10 mM LiI, 1 mM I_2, and 100 mM $LiClO_4$.

Fabrication of DSSCs

To prepare the DSSC working electrodes, the FTO glass plates were first cleaned in a detergent solution using an ultrasonic bath for 15 min, and then rinsed with water and ethanol. A layer of 20 nm-sized anatase TiO_2 nanoparticles (nanopowder, 99.99% trace metals basis (Aldrich)) for the transparent nanocrystalline layer was first coated on the FTO glass plates by the doctor-blade method. After drying the film at 120 °C, another layer of anatase TiO_2 nanoparticles was then deposited as the light scattering layer of the DSSC. The resulting working electrode was composed of a 12 μm-thick transparent TiO_2 nanoparticle layer (particle size: 20 nm) and a 4 μm-thick TiO_2 scattering layer (particle size: 400 nm). The nonporous TiO_2 electrodes were then sequentially heated at 150 °C for 10 min, at 300 °C for 10 min, at 400 °C for 10 min, and finally, at 500 °C for 30 min. After cooling, the nonporous TiO_2 electrodes were immersed into a dye solution at room temperature for 24 hours for dye adsorption. The dye solution was composed of 0.5 mM well-known ruthenium dye N719, [*cis*-di(thiocyanato)-*N*-*N*′-bis(2,2′-bipyridyl-4-carboxylic acid-4′-tetrabutyl-ammonium carboxylate) ruthenium(II)], and 0.5 mM chenodeoxycholic acid (CDCA, as a co-adsorbent) in an acetonitrile–*tert*-butanol mixture (1 : 1). Various CEs for the DSSCs were prepared as described in the previous section. The dye-adsorbed TiO_2 working electrode and a CE were then assembled into a sealed DSSC cell with a sealant spacer between the two electrode plates. A drop of electrolyte solution [0.6 M 1-butyl-3-methylimidazolium iodide (BMII), 0.03 M I_2, 0.5 M 4-*tert*-butylpyridine, and 0.1 M guanidinium thiocyanate in a mixture of acetonitrile–valeronitrile (85 : 15, v/v)] was injected into the cell through a drilled hole. Finally, the hole was sealed using the sealant and a cover glass. An anti-reflection coating film was adhered to the DSSC. A mask with an aperture area of 0.125 cm^2 was used to cover the testing cell during photocurrent–voltage and incident photon-to-current conversion efficiency measurements.

DSSC characterization

The photocurrent–voltage (I–V) characteristics of the DSSCs were measured under illumination of the simulated AM 1.5G solar light from a 550 W xenon lamp solar simulator. The incident light intensity was calibrated to be 100 mW cm^{-2} by using a reference Si photodiode equipped with an IR-cutoff filter (KG-5, Schott) to reduce the spectrum mismatch in the region of 350–750 nm between the simulated light and AM 1.5G to less than 2%. The reference cell is certified by Bunkoh-keiki Co. Ltd, Japan. I–V curves were obtained by applying an external bias voltage to the cell and measuring the generated photocurrent. The incident monochromatic photon-to-current conversion efficiency (IPCE) spectra were measured by using a 150 W xenon arc lamp as the light source coupled to a monochromator. The IPCE data were taken by illuminating monochromatic light on the solar cells (with a wavelength sampling interval of 5 nm from 300 nm to 750 nm) and measuring the short-circuit current of the solar cells. The IPCE measurement was performed under full computer control. Electrochemical impedance spectroscopy (EIS) of the cells was carried out by using an impedance analyzer with a frequency range of 0.1 Hz–1 MHz. In this study, during the impedance measurement, the cell was under constant illumination (AM 1.5G 100 mW cm^{-2}). The impedance of the cell (throughout the frequency range of 0.1 Hz to 1 MHz) was then measured by applying a bias at the open-circuit voltage (V_{OC}) of the cell (namely, under the condition of no DC electric current) and by using an AC amplitude of 10 mV.

Results and discussion

Scheme 1 presents a growth mechanism for the $NbSe_2$ nanostructures. Bulk $NbSe_2$ possesses a hexagonal close packed structure, with the (001) surface being the most densely packed and representing the largest d-spacing plane; thus, the pathway of plastic deformation (fracture) of highly anisotropic $NbSe_2$ prefers to proceed *via* delamination of specific (001) layers.[32,33] Indeed, when beads collide, the fluid squeezed between the two surfaces of contact slows down their approaching motion, due to lubrication, and the materials will be subjected to two distinct mechanical phenomena: either squeezed between two colliding beads or between a bead and a wall, thereby experiencing high pressure and high temperature generated locally in the powder (so-called hot spots) during the milling process.[34,35] During mechanical cleavage, the materials are subjected to severe plastic deformation that exceeds their mechanical strength. In fact, shear and plastic deformations play important roles in the formation of defects and in the occurrence of phase transformations during grinding.[36] The pulling force can easily break the weak van der Waals interactions between layers, resulting in a single or a few layers of smaller size being peeled away from the surface that will be broken-down by fractional forces. Further imposing the materials to shear and friction forces can directly affect both their shape and size (see Fig. S4, ESI†). The resultant layers are repeatedly flattened fractured and welded, the two basic events through which an ultrathin

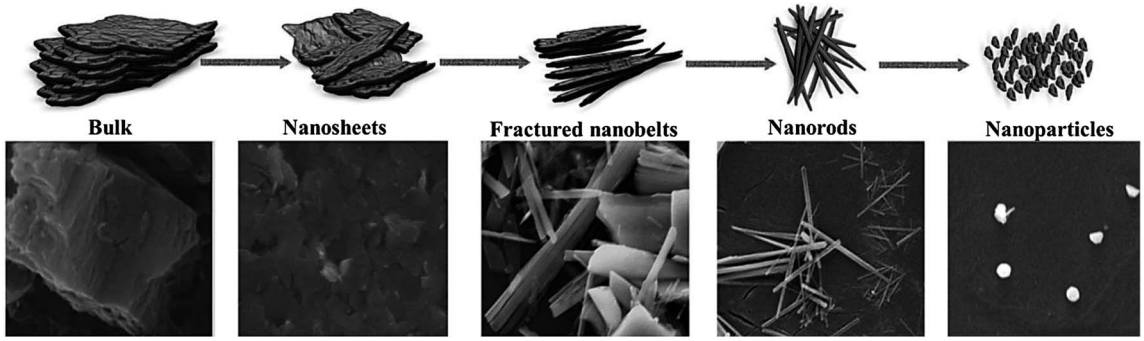

Scheme 1 Schematic representation and the corresponding SEM images of the conversion process: a three-dimensional network of bulk $NbSe_2$ is converted to 2D nanosheets (6 h), 1D nanorods (10 h), and then to 0D nanoparticles (12 h) under the impact and friction of beads.

layer is ruptured along the pathway of the plastic deformation; that is, energy-minimization favors one-dimensional shapes, as observed using microscopes, which can clearly reveal the cleavage process (Fig. 1). In addition, Fig. S5 (ESI†) shows TEM images with a typical high-resolution (HRTEM) image of a fractured nanosheet. The direction of the fractured sheet shows a structure with the [001] crystallographic orientation, in conjunction with the selected-area electron diffraction (SAED) pattern (inset in Fig. S5†) recorded along the (001) zone axis. The (110) direction of the SAED pattern is parallel to the rod axis, and thus shows that fracturing occurs along the (001) direction.

We used SEM and AFM to characterize the morphologies of the as-synthesized $NbSe_2$ nanomaterials. SEM analysis of the pristine $NbSe_2$ (see Fig. S6, ESI†) revealed a very thick (>100 μm), disordered, network arrangement of 2D sheets; in comparison, the ground materials were very thin, separate nanosheets, nanorods, and nanoparticles. Nanosheets have typical lateral dimensions between 100 and 500 nm (Fig. 2a). The nanorods had lengths up to 1.2 μm and diameters ranging from 20 to 100 nm (Fig. 2b), while nanoparticles had an average size of 50–100 nm (Fig. 2c). The AFM images (Fig. 2d–f) also revealed the same dimensions of the nanostructures with the majority having an average thickness of approximately <8 nm for nanosheets, <5 nm for nanorods, and <3 nm for nanoparticles (Fig. S7, ESI†).

We used TEM imaging and diffraction analysis to determine the crystal structures of individual nanostructures. Fig. 3a, d and g present TEM images of a typical nanosheet, nanorod and nanoparticle, respectively. Fig. 3b, e and h provide SAED patterns of flat areas of the nanosheet, nanorod and nanoparticle, respectively. HRTEM of a nanosheet on its edge revealed a spacing of 6.3 Å, which corresponds to the separation between (002) planes and a hexane width of 3.03 Å (Fig. 3c). Hence, the structures of three nanostructures were equivalent and were similar to that of the bulk $NbSe_2$. HRTEM indicated that the individual nanorod and nanoparticle were crystalline (Fig. 3f and i), with the longitudinal axis of the nanorods perpendicular to the [002] direction.[37] The SAED patterns of a number of different nanorods and nanoparticles revealed the same crystallinity as that of the nanosheets. In addition, these SAED patterns were consistent with the XRD patterns (Fig. 4a), which were similar to those of the 2D nanosheets, confirming that no distortion occurred upon flattening and fracturing of these materials. The few-layer nanosheets were typically a few hundred nanometers in length, in agreement with previous reports;[15,18] an ultrathin nanorod having a length of a few hundred nanometers and a width of approximately 25 nm with a thick coating-like amorphous structure on the surface of about 2 nm (Fig. 3f), the nanoparticles having an average size of 50 nm are presented here (Fig. 3d and g) and in the SEM image in Fig. 2b and c. The (001) direction of the SAED pattern is parallel to the rod axis, and thus shows that fracturing occurs along the (001) direction.

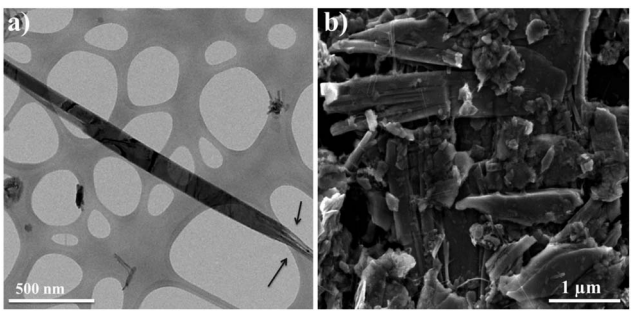

Fig. 1 Microscopy images after one of the conversion stages: (a) TEM, and (b) SEM images of ruptured nanosheets of $NbSe_2$. The starting fractured area in (a) is shown by arrows.

Next, we used XRD to study the phase change of the sample (Fig. 4a). The nearly identical diffraction angles (2θ) of the peaks before and after grinding imply the same degrees of crystallinity, with decreased intensity and broadening of the peaks after grinding, from bulk to sheets, rods and then to particles, being consistent with decreased lateral sizes. The corresponding diffraction peaks for the samples before and after grinding can be indexed to highly crystalline hexagonal $NbSe_2$ (JCPDS file no. 018-0923), at which the four diffraction peaks that are located approximately at 2θ values of 14.00, 30.38, 36.92 and 46.06 can be assigned to the reflections of the (002), (101), (103) and (110) planes, respectively; they suggested that the as-prepared $NbSe_2$ nanomaterials oriented predominantly along the *c*-axis, or the [002] direction,[3,38] consistent with the HRTEM data in Fig. 3. We further confirmed the production of $NbSe_2$ nanomaterials using Raman spectroscopy. The Raman

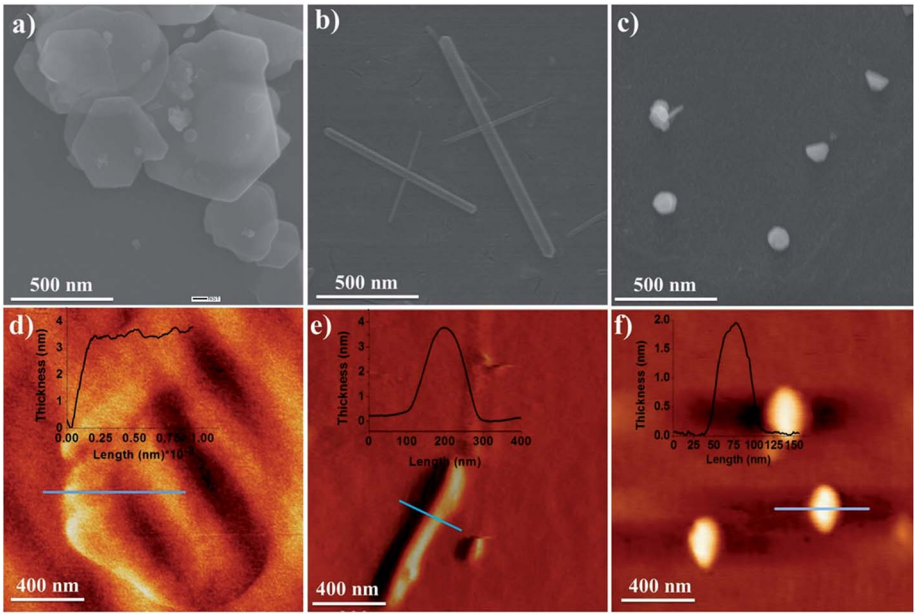

Fig. 2 Morphology of the $NbSe_2$ nanostructures: (a–c) SEM images of different sized nanosheets, nanorods, and nanoparticles, respectively. (d–f) AFM height images of typical nanosheets, nanorods, and nanoparticles, respectively. The insets of AFM images are the corresponding height profiles.

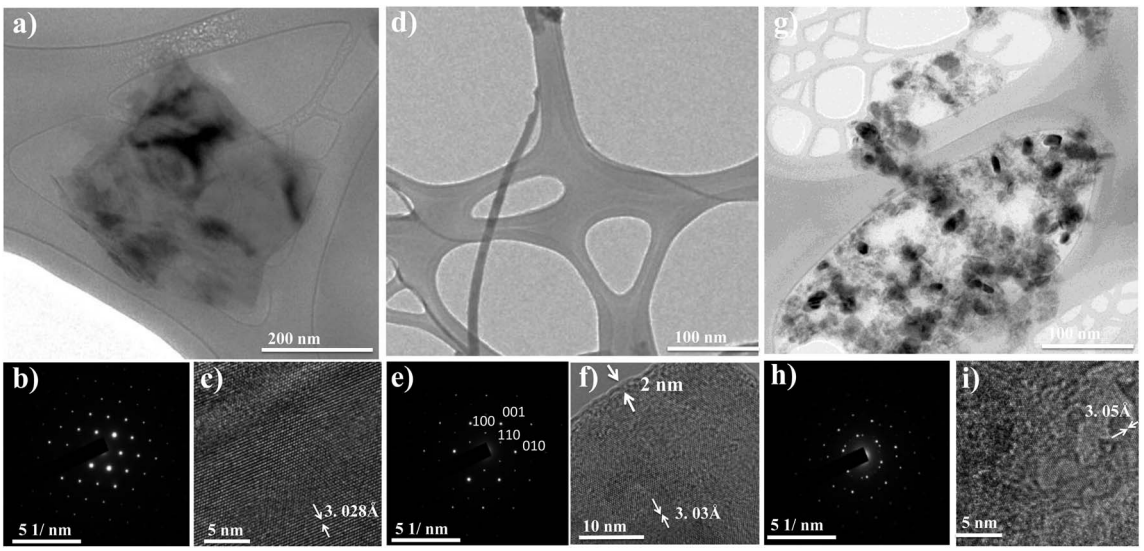

Fig. 3 TEM analysis of $NbSe_2$ nanostructures: (a, d, and g) TEM images, (b, e, and h) SAED patterns, and (c, f, and i) HRTEM images of (a–c) a typical ultrathin $NbSe_2$ nanosheet, (d–f) a typical ultrathin $NbSe_2$ nanorod, and (g–i) a typical $NbSe_2$ nanoparticle.

spectrum ($\lambda_{excitation}$ = 514 nm) in Fig. 4b features three main bands at 220, 267, and 284 cm^{-1} that match well with the values reported previously for $NbSe_2$ single crystals.[39,40] Again, this finding suggests that the crystal structure of $NbSe_2$ was preserved satisfactorily during the milling treatment.

In addition, we used XPS, energy dispersion spectroscopy (EDS), and X-ray fluorescence (XRF) to investigate the stoichiometry of the nanomaterials. We assign the peaks at 202.3 and 205.2 eV in the XPS spectrum of niobium diselenide (Fig. S8, ESI†) to the Nb $3d_{5/2}$ and Nb $3d_{3/2}$ orbitals, respectively, with those at 58 and 55.3 eV representing the Se $3d_{5/2}$ and Se $3d_{3/2}$ orbitals, respectively. These binding energies for the Nb 3d and Se 3d peaks are consistent with oxidation states of Nb^{4+} and Se^{2-} in $NbSe_2$.[37,41] From the EDS spectrum in Fig. S9 (ESI†), we estimated the atomic ratio of Nb to Se in nanorods and nanoparticles to be close to 1 : 2, giving the samples an empirical formula of $NbSe_2$, as confirmed by the XRF-based elemental analysis, which provided a Nb-to-Se ratio of approximately 1 : 2.

To examine whether the grinding process changed the physical properties of the pristine $NbSe_2$ structure, we examined

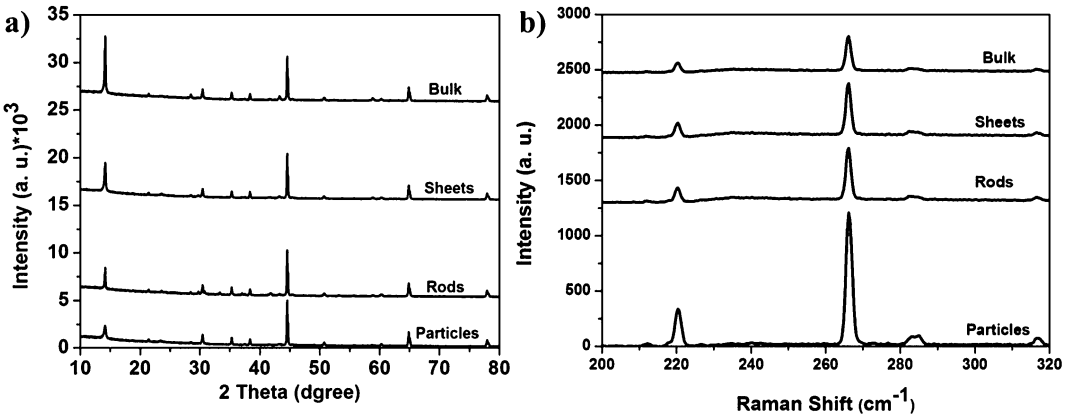

Fig. 4 Structural analysis of $NbSe_2$ nanostructures: (a) powder XRD patterns of bulk $NbSe_2$ and resulting nanostructures (hexagonal; JCPDS: 01-089-4313; $a = b = 3.0$ Å; $c = 12.547$ Å). Periodicity in the c-axis is evident for the bulk material, with a strong (002) peak observed at a value of 2θ of 14°. (b) Raman spectra ($\lambda_{excitation} = 514$ nm) of the bulk $NbSe_2$ and $NbSe_2$ nanostructures.

the superconductivity of the nanostructures. Fig. 5a reveals the temperature-dependent magnetization of these samples in zero-field-cooled AC susceptibility measurements. The existence of superconductivity of the resultant $NbSe_2$ is confirmed by the strong Meissner effects[42] of the nanosheets, rods, and particles at transition temperatures (T_c) of 6.96, 7.084, and 6.89 K, respectively; these values are slightly greater than that of bulk $NbSe_2$ ($T_c = ca.$ 7.2). We observed these transitions consistently

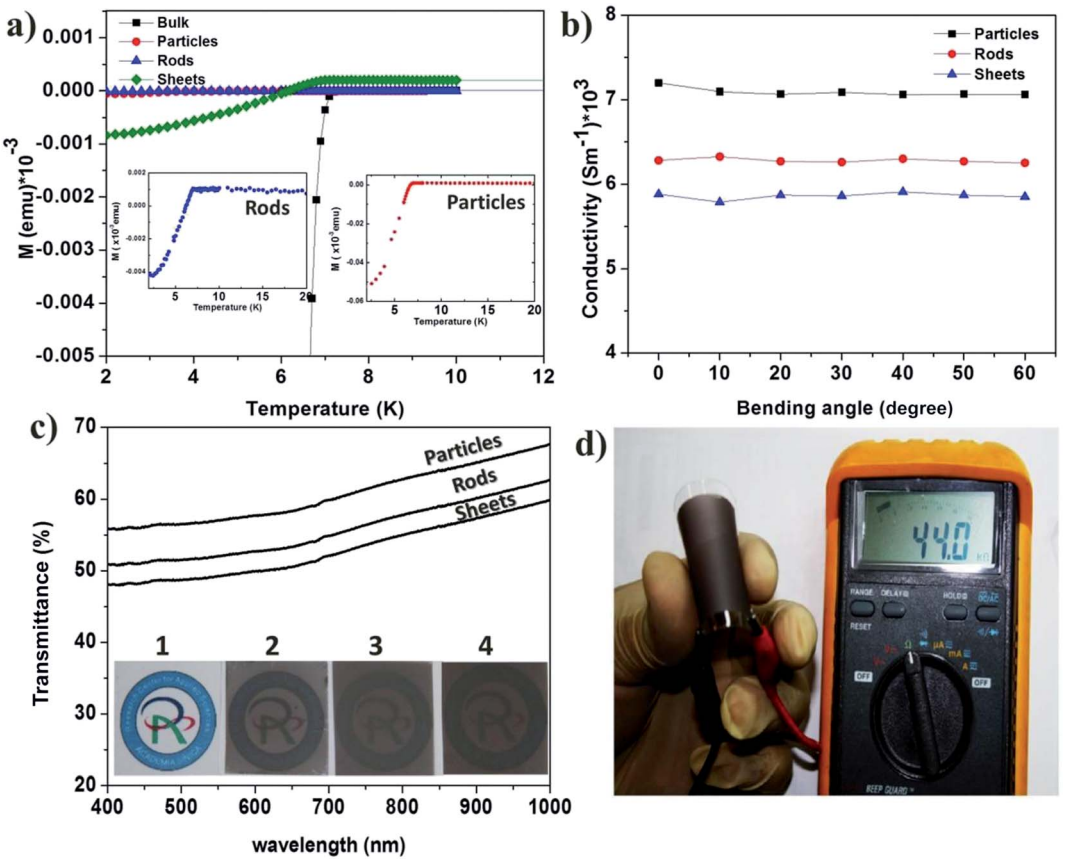

Fig. 5 Superconductivity measurements, bending tests, and transmittance of thin films: (a) magnetic susceptibility plotted with respect to temperature for the pristine $NbSe_2$, the $NbSe_2$ nanosheets, and a powder containing a bundle of $NbSe_2$ nanorods and nanoparticles. Inset: magnified view of the superconductivity transition for the $NbSe_2$ nanorods (left) and nanoparticles (right). (b) Conductivity of a thin film of $NbSe_2$ on a PET substrate, plotted with respect to the bending angle. (c) Transmission spectra of films of the $NbSe_2$ nanostructures. Inset: photograph of the (1) bare PET substrate, (2) film of nanoparticles on PET, (3) film of nanorods on PET, and (4) film of nanosheets on PET. (d) Representative photograph of a film as a flexible electrode subjected to bending.

in all of our samples; unlike the sharp transition of the bulk sample, however, the nanostructures exhibited broadening and depression of their T_c signal amplitudes, possibly as a result of the nanosized effect and contamination by impurities (*e.g.*, O atoms), respectively. This finding also implied that the superconducting phase fraction was small in the nanosized samples.[43]

We used spray coating to prepare very uniform, continuous semitransparent, flexible thin films from the resultant nanostructure materials (Fig. 5d and S10, ESI†). We investigated the flexibility of the thin film by using the conductivity as a parameter and exploring its stability under various bending conditions. Fig. 5b displays the correlation between the bending angle and the conductance of the nanomaterial-containing film. This film exhibited comparable conductance before and after performing the bending test cycle, for example the nanorod film has a conductivity of 5.88 and 5.85 S cm^{-1}, respectively by virtue of its high flexibility and mechanical strength. Fig. 5c presents transmittance spectra of the films on PET substrates. We controlled the thickness of the films to minimize absorption in the visible region while maintaining sufficient conductivity to allow good carrier transport; the film thickness was approximately 230–250 nm (estimated using AFM) and the transmittance at 550 nm was greater than 55%. In addition, we calculated the figures of merit for our transparent conducting films to compare them in the context of other transparent flexible thin films. The figure of merit of the $NbSe_2$ film on PET was approximately 1; this value is superior to those of all published data for the corresponding graphene-containing films[13] (see Section S4 and Fig. S10 and S11, ESI†).

As a proof of principle and to highlight the importance of our findings, we used these $NbSe_2$ nanostructure materials as Pt replacement CEs in DSSCs. Fig. 6a shows the cyclic voltammograms of the I_3^-/I^- redox couple for Pt and $NbSe_2$ CEs. In general, the magnitude of the cathodic current peak represents the catalytic capability of a CE towards reduction of I_3^- in DSSCs. Among the four CEs, the $NbSe_2$ nanosheets exhibited the highest cathodic current. Compared to the Pt CE, the $NbSe_2$ nanosheet CE possesses a larger reduction peak current, indicating better electrocatalytic activity and reversibility in the I_3^-/I^- redox reaction. In contrast, the $NbSe_2$ nanoparticle and nanorod CEs show reduced peak current densities, indicating their lower electrocatalytic activity in the I_3^-/I^- redox reaction. The CV results suggest that depositing $NbSe_2$ nanosheets on FTO glass plates is an effective way to increase the active surface areas of the CEs and thus to enhance their electrocatalytic ability. The enhanced electrocatalytic activity of $NbSe_2$ nanosheet CEs is due to the largest surface areas and better coverage on the FTO glass substrates. The coverage rate of these nanostructures can be calculated from the morphology shown in SEM images (Fig. S12, ESI†). The $NbSe_2$ nanoparticle CE shows a flat film surface, the $NbSe_2$ nanosheet sample exhibits an intercrossed nanosheet conglomeration, and the $NbSe_2$ nanorod sample presents irregular nanorod structures. Among the

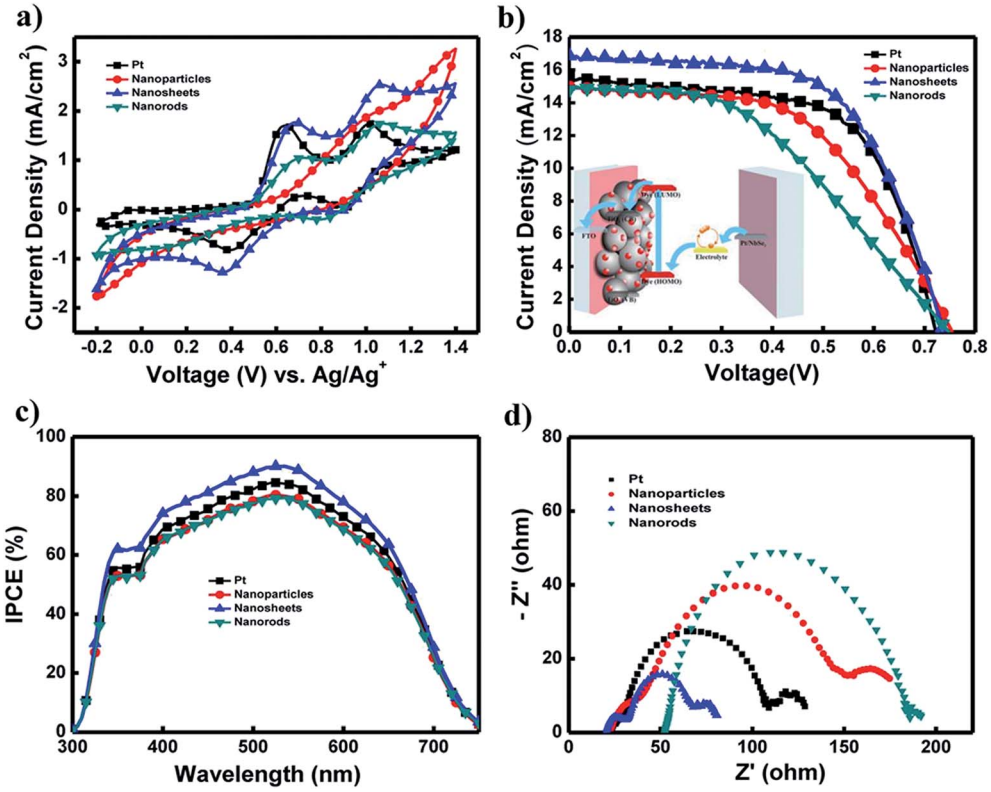

Fig. 6 (a) Cyclic voltammograms of Pt and various $NbSe_2$ CEs. (b) *J*–*V* curves, (c) IPCE curves, and (d) EIS Nyquist plots of DSSCs based on Pt and various $NbSe_2$ CEs. The inset of (b) is the schematic representation of the DSSC device structure with an energy level diagram of the component materials used for device fabrication.

three $NbSe_2$ CEs, the $NbSe_2$ nanosheet CE exhibits the largest surface area and best coverage on the FTO glass substrates.

The photovoltaic characteristics of Pt, $NbSe_2$ nanoparticles, nanosheets, and nanorods as the CEs in DSSCs were evaluated with a sandwich DSSC cell. Fig. 6b and c show the *I–V* and IPCE characteristics, respectively, of the DSSCs using various CEs and the device parameters are summarized in Table 1.

The DSSC based on the Pt CE shows an overall conversion efficiency of 7.01%. Under the same conditions, DSSCs based on $NbSe_2$ nanosheet CEs exhibit a higher power conversion efficiency of 7.73%. On the other hand, DSSCs based on $NbSe_2$ nanoparticle and nanorod CEs show inferior conversion efficiencies of 6.27% and 5.05%, respectively. This lower efficiency mainly comes from a relatively low fill factor (FF) owing to the small surface area and low coverage on FTO substrates. Such results indicate that the $NbSe_2$ nanosheets could provide cost-effective CEs alternative to the noble metal Pt in DSSCs due to their high surface area and coverage.

Further investigation of the higher device parameters of $NbSe_2$ nanosheet CEs is given by using the IPCE spectra of the DSSCs based on various CEs as shown in Fig. 6c. Among these four CEs, DSSCs based on $NbSe_2$ nanosheets exhibit the best spectral response. The peak increases from ~84% of the DSSCs based on Pt, to ~89% of the DSSCs based on $NbSe_2$ nanosheets. In contrast, DSSCs based on $NbSe_2$ nanoparticles and nanorod CEs show relatively lower IPCE peak values, indicating their inferior short-circuit current values. The IPCE results are in accordance with the short-circuit currents of the DSSCs.

The DSSCs were further characterized by electrochemical impedance spectroscopy (EIS). EIS is a useful tool for characterizing important interfacial charge-transfer processes in DSSCs, such as the electron transfer/charge recombination at the TiO_2/dye/electrolyte interface, electron transport in the TiO_2 electrode, electron transfer at the CE, and I_3^- transport in the electrolyte, *etc.*[44,45] Fig. 6d shows the EIS Nyquist plots (*i.e.*, minus imaginary part of the impedance, $-Z''$, *vs.* the real part of the impedance, Z', when sweeping the frequency) for DSSCs based on various CEs. For the frequency range investigated (0.1 Hz to 1 MHz), three regimes are generally distinguished: a small semicircle in the lowest frequency range (~0.1 Hz to 1 Hz), a larger semicircle in the middle frequency range (~1 Hz to 1 kHz), and another smaller semicircle in the highest frequency range (>1 kHz). With the bias illumination and voltage applied, the small semicircle at the lowest frequencies is associated with ion diffusion in the electrolyte; the larger semicircle at middle frequencies corresponds to the charge-transfer processes at the TiO_2/dye/electrolyte interface, while the smaller semicircle at the highest frequencies corresponds to the charge-transfer processes at the CE/electrolyte interface.[30] Among these four CEs, the smallest width of the middle-frequency semicircle in the EIS was observed in the DSSCs based on $NbSe_2$ nanosheet CEs, which indicates the most efficient electrocatalytic activity for I_3^- reduction and electron generation and thus larger electron population at their TiO_2/dye/electrolyte interface. The EIS results are in good agreement with results of the short-circuit currents and the overall power conversion efficiencies of the DSSCs.

Table 1 Characteristics of DSSCs fabricated using various CEs. PCEs were averaged over 10 solar cells

Counter electrode	J_{sc} (mA cm^{-2})	V_{oc} (V)	Fill factor	Efficiency (%)
Pt	15.59	0.72	0.62	7.01
$NbSe_2$ nanoparticles	14.93	0.75	0.55	6.27
$NbSe_2$ nanosheets	16.85	0.74	0.62	7.73
$NbSe_2$ nanorods	14.85	0.74	0.46	5.05

Conclusion

In conclusion, we have developed a novel and feasible approach with control over the milling time for converting layered bulk $NbSe_2$ to low dimensional materials under the influence of mechanical forces. This very simple technique has the potential for scaling up to mass production at low cost, offering a promising opportunity to produce nanomaterials in volumes required for real-world applications. When these nanostructure materials were used as CEs in DSSCs, the $NbSe_2$ nanosheet CE showed the highest power conversion efficiency compared to nanorods, nanoparticles, and Pt CEs. Such results indicate that the $NbSe_2$ nanosheets could provide cost-effective CEs alternative to the noble metal Pt in DSSCs due to their high surface area and coverage. In addition, this approach should lead to the preparation of thin films of inorganic layered compounds for application in batteries and other devices, as well as to the production of a wide range of hybrids with tunable conductivity, attractive thermoelectric properties, and enhanced mechanical properties.

Acknowledgements

We thank the National Science Council (NSC), Taiwan (NSC 102-2221-E-001-029-MY2 and NSC 102-2221-E-259-025), for the financial support. Dr Chu is grateful for the technical support from Nano Core, the Core Facilities for Nanoscience and Nanotechnology at Academia Sinica in Taiwan.

References

1 A. K. Geim and K. S. Novoselov, *Nat. Mater.*, 2007, **6**, 183–191.
2 M. Xu, T. Liang, M. Shi and H. Chen, *Chem. Rev.*, 2013, **113**, 3766–3798.
3 X. Huang, Z. Zeng and H. Zhang, *Chem. Soc. Rev.*, 2013, **42**, 1934–1946.
4 M. Chhowalla, H. S. Shin, G. Eda, L.-J. Li, K. P. Loh and H. Zhang, *Nat. Chem.*, 2013, **5**, 263–275.
5 L. Rapoport, A. Moshkovich, V. Perfilyev, A. Laikhtman, I. Lapsker, L. Yadgarov, R. Rosentsveig and R. Tenne, *Tribol. Lett.*, 2011, **45**, 257–264.
6 V. V. Ivanovskaya, A. N. Enyashin, N. I. Medvedeva and A. L. Ivanovskii, *Phys. Status Solidi B*, 2003, **238**, R1–R4.
7 H. Liu, D. Su, R. Zhou, B. Sun, G. Wang and S. Z. Qiao, *Adv. Energy Mater.*, 2012, **2**, 970–975.
8 M. A. Ibrahem, T.-w. Lan, J. K. Huang, Y.-Y. Chen, K.-H. Wei, L.-J. Li and C. W. Chu, *RSC Adv.*, 2013, **3**, 13193–13202.

9 J. Guo, Y. Shi, C. Zhu, L. Wang, N. Wang and T. Ma, *J. Mater. Chem. A*, 2013, **1**, 11874–11879.
10 C. Ataca, H. Şahin and S. Ciraci, *J. Phys. Chem. C*, 2012, **116**, 8983–8999.
11 B. Radisavljevic, A. Radenovic, J. Brivio, V. Giacometti and A. Kis, *Nat. Nanotechnol.*, 2011, **6**, 147–150.
12 K. J. Reynolds, G. L. Frey and R. H. Friend, *Appl. Phys. Lett.*, 2003, **82**, 1123.
13 S. Alkis, T. Özta, L. E. Aygün, F. Bozkurt, A. K. Okyay and B. Ortaç, *Opt. Express*, 2012, **20**, 21815–21820.
14 R. J. Smith, P. J. King, M. Lotya, C. Wirtz, U. Khan, S. De, A. O'Neill, G. S. Duesberg, J. C. Grunlan, G. Moriarty, J. Chen, J. Wang, A. I. Minett, V. Nicolosi and J. N. Coleman, *Adv. Mater.*, 2011, **23**, 3944–3948.
15 J. N. Coleman, M. Lotya, A. O'Neill, S. D. Bergin, P. J. King, U. Khan, K. Young, A. Gaucher, S. De, R. J. Smith, I. V. Shvets, S. K. Arora, G. Stanton, H. Y. Kim, K. Lee, G. T. Kim, G. S. Duesberg, T. Hallam, J. J. Boland, J. J. Wang, J. F. Donegan, J. C. Grunlan, G. Moriarty, A. Shmeliov, R. J. Nicholls, J. M. Perkins, E. M. Grieveson, K. Theuwissen, D. W. McComb, P. D. Nellist and V. Nicolosi, *Science*, 2011, **331**, 568–571.
16 A. Meerschaut and C. Deudon, *Mater. Res. Bull.*, 2001, **36**, 1721–1727.
17 S. Lebègue and O. Eriksson, *Phys. Rev. B: Condens. Matter Mater. Phys.*, 2009, **79**, 115409.
18 G. Cunningham, M. Lotya, C. S. Cucinotta, S. Sanvito, S. D. Bergin, R. Menzel, M. S. P. Shaffer and J. N. Coleman, *ACS Nano*, 2012, **6**, 3468–3480.
19 K. Zhou, S. Jiang, C. Bao, L. Song, B. Wang, G. Tang, Y. Hu and Z. Gui, *RSC Adv.*, 2012, **2**, 11695–11703.
20 Z. Zeng, T. Sun, J. Zhu, X. Huang, Z. Yin, G. Lu, Z. Fan, Q. Yan, H. H. Hng and H. Zhang, *Angew. Chem., Int. Ed. Engl.*, 2012, **51**, 9052–9056.
21 Y. Du, Z. Yin, J. Zhu, X. Huang, X. J. Wu, Z. Zeng, Q. Yan and H. Zhang, *Nat. Commun.*, 2012, **3**, 1177.
22 Y.-H. Lee, X.-Q. Zhang, W. Zhang, M.-T. Chang, C.-T. Lin, K.-D. Chang, Y.-C. Yu, J. T.-W. Wang, C.-S. Chang, L.-J. Li and T.-W. Lin, *Adv. Mater.*, 2012, **24**, 2320–2325.
23 Z. Liu, S. Peng, Q. Xie, Z. Hu, Y. Yang, S. Zhang and Y. Qian, *Adv. Mater.*, 2003, **15**, 936–940.
24 Z. He, S. H. Yu, X. Zhou, X. Li and J. Qu, *Adv. Funct. Mater.*, 2006, **16**, 1105–1111.
25 C.-C. Lin, W.-F. Lee, M.-Y. Lu, S.-Y. Chen, M.-H. Hung, T.-C. Chan, H.-W. Tsai, Y.-L. Chueh and L.-J. Chen, *J. Mater. Chem.*, 2012, **22**, 7098–7103.
26 R. J. Mehta, C. Karthik, W. Jiang, B. Singh, Y. Shi, R. W. Siegel, T. Borca-Tasciuc and G. Ramanath, *Nano Lett.*, 2010, **10**, 4417–4422.
27 W. Zhao, M. Fang, F. Wu, H. Wu, L. Wang and G. Chen, *J. Mater. Chem.*, 2010, **20**, 5817.
28 B. O'Regan and M. Gratzel, *Nature*, 1991, **353**, 737–740.
29 S. Thomas, T. G. Deepak, G. S. Anjusree, T. A. Arun, S. V. Nair and A. S. Nair, *J. Mater. Chem. A*, 2014, **2**, 4474–4490.
30 S. Ahmad, E. Guillen, L. Kavan, M. Gratzel and M. K. Nazeeruddin, *Energy Environ. Sci.*, 2013, **6**, 3439–3466.
31 X. Yang, S. Zhang, K. Zhang, J. Liu, C. Qin, H. Chen, A. Islam and L. Han, *Energy Environ. Sci.*, 2013, **6**, 3637–3645.
32 J.-M. Li, *Appl. Phys. A: Mater. Sci. Process.*, 2009, **99**, 229–235.
33 J.-M. Li, *Nano Lett.*, 2008, **8**, 1382–1385.
34 M. Bodaghi, A. R. Mirhabibi, H. Zolfonun, M. Tahriri and M. Karimi, *Phase Transitions*, 2008, **81**, 571–580.
35 R. Gers, E. Climent, D. Legendre, D. Anne-Archard and C. Frances, *Chem. Eng. Sci.*, 2010, **65**, 2052–2064.
36 V. Sepelak, S. Begin-Colin and G. Le Caer, *Dalton Trans.*, 2012, 11927–11948.
37 N. D. Boscher, C. J. Carmalt and I. P. Parkin, *Eur. J. Inorg. Chem.*, 2006, 1255–1259.
38 S. Bose, P. Raychaudhuri, R. Banerjee, P. Vasa and P. Ayyub, *Phys. Rev. Lett.*, 2005, **95**, 147003.
39 Y. Wu, M. An, R. Xiong, J. Shi and Q. M. Zhang, *J. Phys. D: Appl. Phys.*, 2008, **41**, 175408.
40 N. Staley, J. Wu, P. Eklund, Y. Liu, L. Li and Z. Xu, *Phys. Rev. B: Condens. Matter Mater. Phys.*, 2009, **80**, 184505.
41 S. Chiang, G. K. Wertheim and F. J. DiSalvo, *Solid State Commun.*, 1976, **19**, 75–78.
42 K. H. Bennemann and J. B. Ketterson, *The Physics of Superconductors: Vol. II: Superconductivity in Nanostructures, High-Tc and Novel Superconductors, Organic Superconductors*, Springer, 2004.
43 S. Bose, P. Raychaudhuri, R. Banerjee, P. Vasa and P. Ayyub, *Phys. Rev. Lett.*, 2005, **95**, 147003.
44 F. Malara, M. Manca, M. Lanza, C. Hubner, E. Piperopoulos and G. Gigli, *Energy Environ. Sci.*, 2012, **5**, 8377–8383.
45 L. Yi, Y. Liu, N. Yang, Z. Tang, H. Zhao, G. Ma, Z. Su and D. Wang, *Energy Environ. Sci.*, 2013, **6**, 835–840.

